Geophysical Research Letters

RESEARCH LETTER
10.1029/2023GL103480

Key Points:

- An earthquake doublet of M_W 7.9 and M_W 7.6 ruptured multiple segments and curved faults
- Initial splay fault rupture triggered a large M_W 7.9 rupture involving pulses of back-propagating supershear rupture
- Multi-scale rupture growth in a complex fault network may facilitate diverse rupture behaviors and triggering interactions in the doublet

Supporting Information:

Supporting Information may be found in the online version of this article.

Correspondence to:

R. Okuwaki,
rokuwaki@geol.tsukuba.ac.jp

Citation:

Okuwaki, R., Yagi, Y., Taymaz, T., & Hicks, S. P. (2023). Multi-scale rupture growth with alternating directions in a complex fault network during the 2023 south-eastern Türkiye and Syria earthquake doublet. *Geophysical Research Letters*, *50*, e2023GL103480. https://doi.org/10.1029/2023GL103480

Received 3 MAR 2023
Accepted 1 JUN 2023

Multi-Scale Rupture Growth With Alternating Directions in a Complex Fault Network During the 2023 South-Eastern Türkiye and Syria Earthquake Doublet

Ryo Okuwaki[1], Yuji Yagi[1], Tuncay Taymaz[2], and Stephen P. Hicks[3]

[1]Faculty of Life and Environmental Sciences, University of Tsukuba, Tsukuba, Japan, [2]Department of Geophysical Engineering, The Faculty of Mines, Istanbul Technical University, Istanbul, Türkiye, [3]Department of Earth Sciences, University College London, London, UK

Abstract A devastating doublet of earthquakes with moment magnitude M_W 7.9 and M_W 7.6 earthquakes contiguously occurred in SE Türkiye near the NW border of Syria. Here we perform a potency-density tensor inversion to simultaneously estimate rupture evolution and fault geometry for the doublet. We find the initial M_W 7.9 earthquake involved discrete episodes of supershear rupture and back-rupture propagation, and was triggered by initial rupture along a bifurcated splay of the East Anatolian Fault. The second M_W 7.6 event was triggered by the earlier M_W 7.9 event, and it involved more extensive supershear rupture along a favorably curved fault, and was likely stopped by geometric barriers at the fault ends. Our results highlight the multi-scale cascading rupture growth across the complex fault network that affects the diverse rupture geometries of the 2023 Türkiye earthquake doublet, contributing to the strong ground shaking and associated devastation.

Plain Language Summary On 6 February 2023, devastating dual earthquakes; moment magnitude 7.9 and 7.6 events struck southern Türkiye near the northern border of Syria. The two earthquakes were only separated ~90 km and ~9 hr apart. The strong shaking from the two earthquakes caused significant damage to the buildings and people, having caused over 50,000 fatalities in Türkiye and Syria. The source region is where the Anatolian, Arabian and African plates meet, developing the network of faults that hosted the large devastating earthquakes. Seismological analyses using observed seismic waveforms are effective for rapidly estimating how the rupture of the two earthquakes evolves over such distinctively oriented and possibly segmented faults. We use the globally observed seismic records to simultaneously estimate rupture evolution and fault geometry of the earthquake doublet. We find the sequence of both earthquakes involves curved and segmented fault ruptures, including the back-propagating rupture for the initial earthquake, which is facilitated by the complex active fault network. The 2023 earthquake doublet displays the irregular rupture evolution and diverse triggering behaviors both in a single event and across the earthquake sequence, which provide critical inputs in both our understanding of earthquake-rupture dynamics and better assessment of future damaging earthquakes.

1. Introduction

The Eastern Mediterranean region is one of Earth's most active tectonic environments, where the Anatolian plate is extruded westward, escaping from the collision between the Arabian and Eurasian plates (McKenzie, 1972; Taymaz, Eyidogan, & Jackson, 1991; Taymaz, Jackson, & McKenzie, 1991; Taymaz et al., 2004). To the south-east of the Anatolian plate, the left-lateral East Anatolian Fault (EAF), along with the right-lateral North Anatolian Fault (NAF), accommodates the extrusion of the Anatolian plate (Jackson & McKenzie, 1984; Taymaz, Eyidogan, & Jackson, 1991; Taymaz et al., 2021). The EAF forms an intra-continental transform fault, which separates the Anatolian and Arabian plates (Figure 1). Although the EAF has been less seismically active than that around the NAF since instrumental-based catalogs started (e.g., Ambraseys, 1989), the EAF has hosted magnitude M 7+ earthquakes in the past, for example, an M 7.1 1893 in Çelikhan, an M 7.4 1513 in Pazarcık, and an M 7.5 in 1822 to the east of Hassa (Ambraseys, 1989; Ambraseys & Jackson, 1998; Duman & Emre, 2013). Most recently, in 2020, a moment magnitude M_W 6.8 Doğanyol–Sivrice earthquake broke the region east of the 1893 M 7.1 earthquake (Melgar et al., 2020; Pousse-Beltran et al., 2020; Ragon et al., 2021; Taymaz et al., 2021), located to the north-east of the 2023 earthquakes focused on in this study. The EAF is recognized to have multiple geometrically segmented faults and a series of bends, step-overs, and sub-parallel faults, leading to complex fault

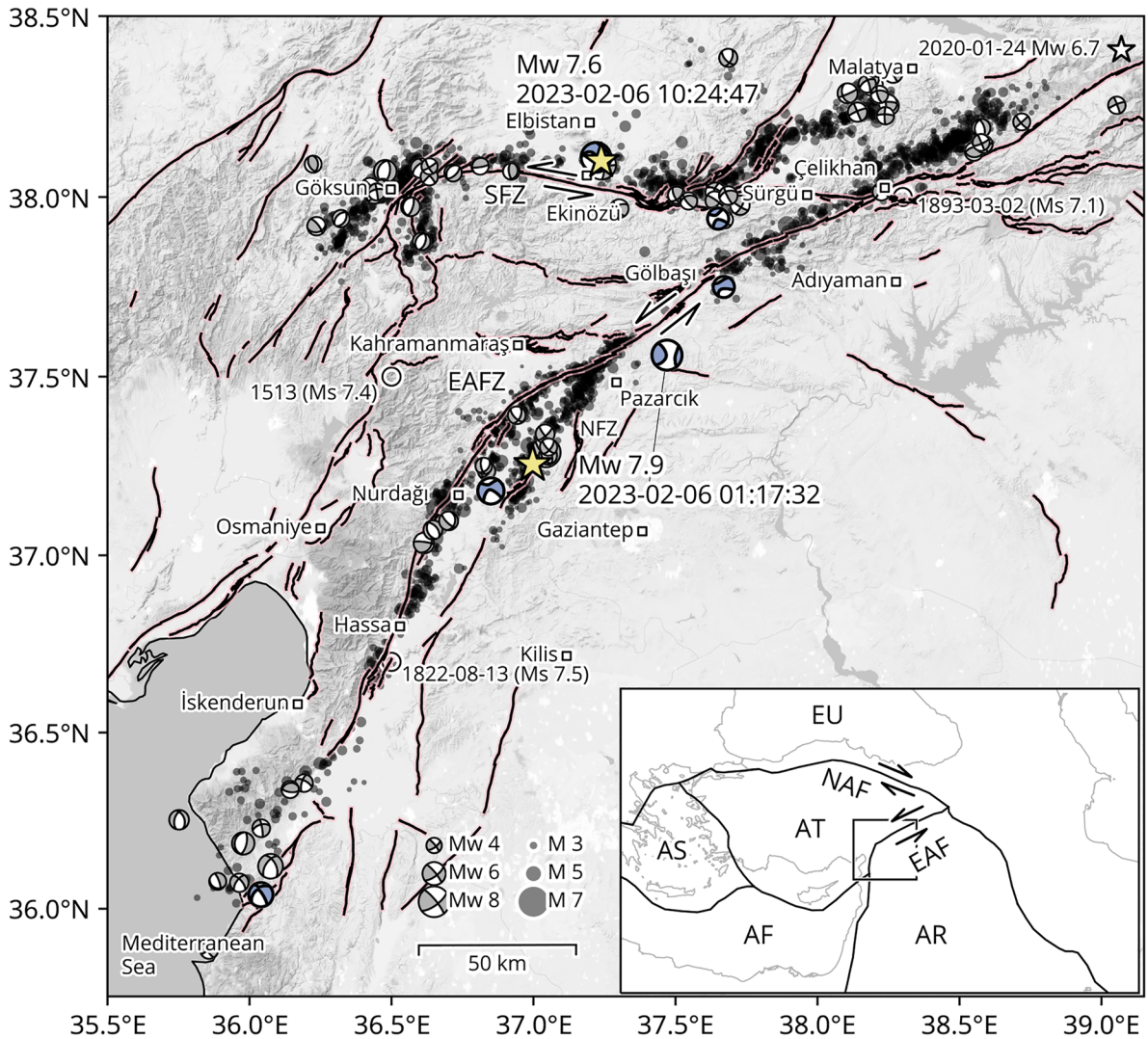

Figure 1. Summary of the study region. The yellow stars are the relocated epicenters of the M_W 7.9 and M_W 7.6 earthquakes. The dots are the relocated aftershocks ($M \geq 1.1$) from 2023–02–06 01:17:32 (UTC) to 2023-02-16 21:35:55 (UTC) (after Melgar et al., 2023). The blue beachballs are the Global Centroid Moment Tensor solutions (Dziewonski et al., 1981; Ekström et al., 2012) and the gray beachballs are the focal mechanisms determined by the AFAD (AFAD Focal Mechanism Solution, 2023) during the 2023 earthquake sequence. The active faults are from Emre et al. (2018), including the East Anatolian Fault (EAF) Zone (EAFZ), Sürgü Fault Zone (SFZ), and Narlıdağ fault zone (NFZ). The square markers locate major provinces and towns. The white star is the epicenter of the 2020 M_W 6.7 Doğanyol–Sivrice earthquake (Taymaz et al., 2021). The circles are the epicenters of the historical earthquakes (Ambraseys, 1989; Ambraseys & Jackson, 1998). The basemap tiles (terrain) including the administrative boundaries are provided by Stamen Design (under CC BY 3.0 license) and OpenStreetMap (under ODbL license). The inset map shows the boundaries between Aegean Sea (AS), African (AF), Anatolian (AT), Arabian (AR), and Eurasian (EU) plates (Bird, 2003). The arrows denote the relative motion of the EAF and the North Anatolian Fault. The square box outlines the map extent of this figure.

networks (Figure 1) (e.g., Duman & Emre, 2013). This complexity is particularly evident in southern Türkiye, where the EAF connects to the triple junction of the Anatolian, Arabian and African plates, and the main plate boundary merges into the Dead Sea Fault zone to the south. This diffuse zone of deformation manifests as a rotation in the strike of the main EAF from NE-SW in the NE to SSW-NNE near the town of Pazarcık, SW Kahramanmaraş province (Figure 1). To the north of Kahramanmaraş province, the EW-oriented Sürgü fault zone (SFZ), obliquely branches from the main EAF (Arpat & Saroglu, 1972; Duman & Emre, 2013; Duman et al., 2020; Taymaz, Eyidogan, & Jackson, 1991).

Two devastating earthquakes with M 7.7 and M 7.6 (AFAD, 2023) occurred on 6 February 2023 near the SW end of the EAF in Nurdağı-Pazarcık segment, SE Türkiye near the northern border of Syria (AFAD, 2023; Barbot et al., 2023; Delouis et al., 2023; Melgar et al., 2023; Rosakis et al., 2023; Zahradník et al., 2023). In the

following, we refer to the magnitude of those earthquakes as M_W 7.9 and M_W 7.6, respectively, based on our own estimates that will be presented in the following sections. The two earthquakes occurred only ∼9 hr and ∼90 km apart (Figure 1). The epicenters reported by AFAD (2023) show that the initial M_W 7.9 earthquake seems to have initiated off the main EAF strand in the Narlıdağ fault zone (Duman & Emre, 2013), lying ∼15 km to the east (Figure 1). In contrast, the secondary M_W 7.6 earthquake lies near the SFZ (Figure 1). The relocated aftershocks (Melgar et al., 2023) seemingly align with the main EAF strand and the northern strand of the EAF, whilst some other linear trends and clusters can be seen off the main EAF segment. For example, around the epicenter of the initial M_W 7.9 earthquake, some aftershocks appear to branch away from the main EAF (Figure 1). Global Centroid Moment Tensor solutions (Dziewonski et al., 1981; Ekström et al., 2012) for the two earthquakes have oblique left-lateral strike-slip faulting. The fault orientations of the two solutions are apparently consistent with the bulk orientations of the main EAF segment and the SFZ respectively (Figure 1), however, the moment tensors show moderately-high non-double couple components of 42% and 57%.

The geometric complexity of the EAF and the adjacent fault networks, the apparent offset of the initial M_W 7.9 epicenter from the main EAF strand, the high non-double couple components of the GCMT solutions, and the aftershock distribution with diverse orientations collectively suggest the earthquake sequence involved complexity in both rupture evolution and fault geometry (Abercrombie et al., 2003; Okuwaki & Fan, 2022; Okuwaki et al., 2021). In general, geometric complexities of a fault system are known to control rupture speed and direction, and triggering of separated fault segments (Das & Aki, 1977; Huang, 2018; Kase & Day, 2006; Yıkılmaz et al., 2015). There is also growing observational evidence of rupture irregularity within fault damage zones in different tectonic regimes, such as transient supershear ruptures across fault bends (Bao et al., 2019; Socquet et al., 2019), triggering of ruptures with different faulting styles and on different segments (Nissen et al., 2016; Ruppert et al., 2018; Wei et al., 2011), and apparent rupture back-propagation or re-rupture (Gallovič et al., 2020; Hicks et al., 2020; Yagi et al., 2023; Yamashita, Yagi, & Okuwaki, 2022). Such diverse rupture behavior in different tectonic environments and fault zones gives fundamental inputs that deepen and accelerate our understanding of earthquake-source physics and the knock-on effects on strong ground motion. However, it has been challenging for seismologists to rigorously retrieve rupture complexity that should be recorded in rich waveform datasets, because of the necessity of assumptions involving the fault geometry and rupture direction, which are often not necessarily required by the data itself and sometimes bias the interpretation of the earthquake source process. The methodological difficulties in analyzing geometrically complex earthquakes are a huge obstacle in our understanding of earthquake source physics, but also hinder rapid and robust response, especially for destructive events like the 2023 SE Türkiye and Syria earthquake sequence, and assessing of future earthquake (e.g., aftershock) hazard in the short-to-medium term (e.g., Dal Zilio & Ampuero, 2023; Hall, 2023; Hussain et al., 2023).

Here we report a narrative of rupture evolution of the two M_W 7.9 and M_W 7.6 earthquakes using teleseismic *P*-waveforms observed globally at broadband seismic stations. We find the two nearby earthquakes ruptured multiple segments and branches of the EAF, and involving curved faults, which likely influenced slip acceleration and deceleration during discrete rupture episodes. Most notably, the initial M_W 7.9 earthquake involved an apparent back-propagating supershear rupture through and beyond the hypocenter area, which should be responsible for the series of triggering of sub-events in their unfortunately favorable orientation.

2. Materials and Methods

In general, finite fault inversion estimates the spatio-temporal slip distribution on an assumed fault plane (Hartzell & Heaton, 1983; Olson & Apsel, 1982). Such modeled fault geometries may be refined using field observations and satellite imagery that captures the surface deformation. However, strictly prescribing fault geometry may bias our interpretation of the solution, because limiting model flexibility can mask subtle rupture details and fault geometries beyond what can sometimes be observed at the surface (e.g., Shimizu et al., 2020). Similar problems may arise when strict assumptions are made about kinematic information such as rupture velocity and direction.

In this study, we perform a recently developed potency-density tensor inversion (Shimizu et al., 2020; Yamashita, Yagi, Okuwaki, Shimizu, et al., 2022) for both the M_W 7.9 and M_W 7.6 earthquakes using teleseismic *P*-waves. Our approach is particularly effective for analyzing complex earthquake sequences, because it does not require any detailed assumptions about the fault geometry, but rather, we simultaneously solve for fault geometry and slip as data requires. In this study, we configured the model-space geometry based on the recognized active faults (Emre et al., 2018) and the relocated aftershocks (Melgar et al., 2023) around the source region of the

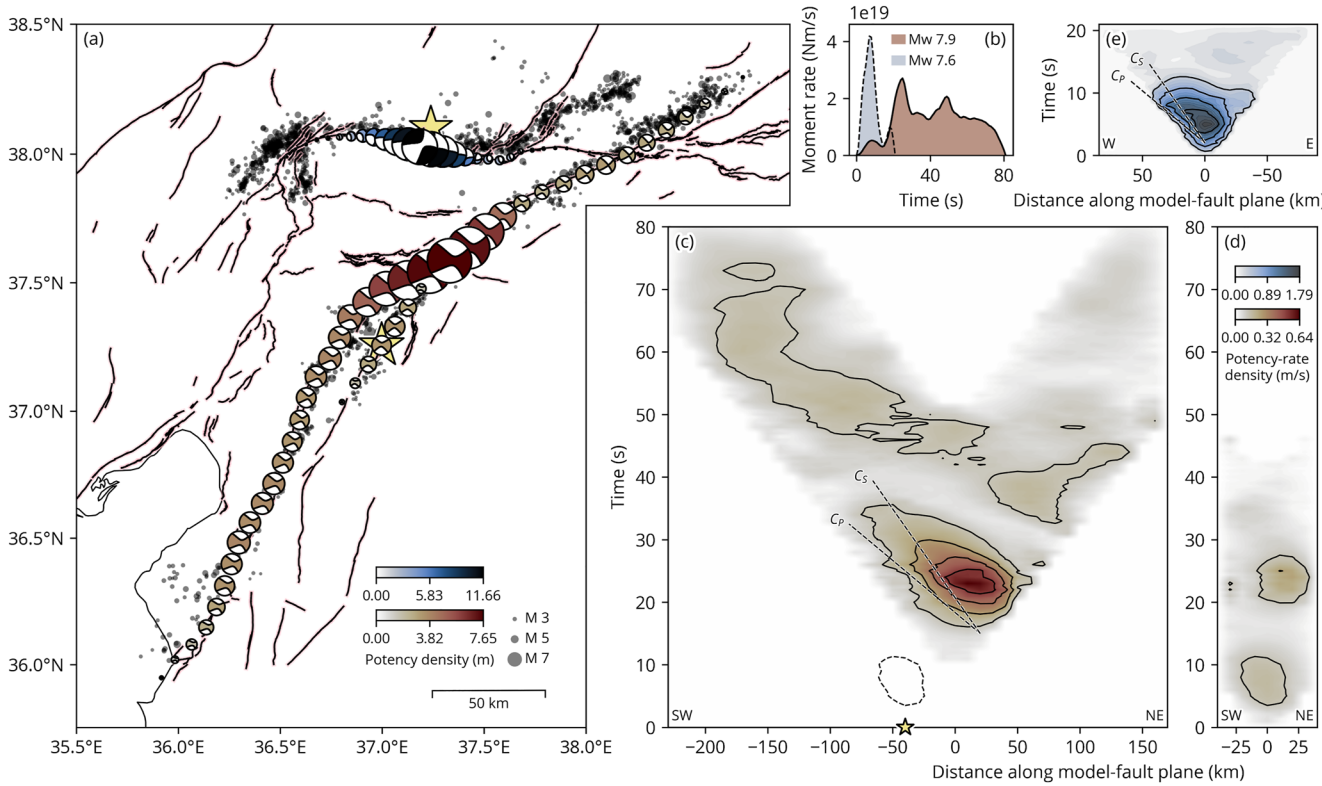

Figure 2. Summary of our solutions for the M_W 7.9 and M_W 7.6 earthquakes. (a) The beachball shows the lower-hemisphere projection of the moment tensor calculated by integrating the potency-rate density tensors with respect to time at each source element, with its size scaled with the potency density. Only the moment tensors with the maximum potency density along depth are shown. A full set of the potency-density tensors are shown in Figure S4 in Supporting Information S1. The stars, dots, and lines are the same as shown in Figure 1. (b) The moment-rate functions. The right panels show the spatiotemporal distributions of the potency-rate density for (c, d) the M_W 7.9 and (e) the M_W 7.6 earthquakes, projected along the non-planar model faults. The "0" on the *X*-axis of panel (c) corresponds to the location of junction between the splay fault and the main East Anatolian Fault (EAF), while "0" of panel (d) corresponds to the initial rupture point on the splay fault. The star shows the location of the source element on the EAF that is closest to the initial rupture point on the splay fault. The dashed contours show the potency-rate density on the splay fault during OT+0–15 s projected onto the approximate location on the main EAF model domain. The panel (d) is the splay fault domain for the M_W 7.9 earthquake. The abscissa shows the distance along the model fault. The dashed lines of C_P (6.0 km/s) and C_S (3.5 km/s) represent the reference *P*- and *S*-wave velocities near the source region from the first layer of Table S1 in Supporting Information S1. The black contours are drawn at every 0.13 m/s (lower panels) and 0.36 m/s (upper panel) for the M_W 7.9 and the M_W 7.6 earthquakes, respectively. The panel (d) is flipped horizontally so that it can intuitively be compared with a map view of the corresponding model.

two earthquakes (Figure S3 in Supporting Information S1). Regardless of this model-space parameterization, one strength of our approach is that the potency tensors at each source element remain flexible to represent fault geometry that deviates from the prescribed model-fault geometry. This modeling flexibility is particularly advantageous for analyzing an earthquake in a complex fault zone, where there are multiple segments of faults with different orientations, and possible supershear ruptures, which are likely factors for the 2023 SE Türkiye earthquake doublet given the strike-slip configuration and known structure of the EAF.

We adopted a maximum rupture-front speed of 4 km/s based on the upper limit of *S*-wave velocity near the source (Table S1 in Supporting Information S1) so that the model space can capture possible supershear rupture or inter-subevent dynamic triggering. We also tested a faster maximum rupture-front speed at 5 km/s, and the key features of the rupture process that we discuss next were reproduced (Figure S11 in Supporting Information S1). We also adopted a sufficiently long maximum slip duration at each source element of 42 s and a total source duration of 80 s for the initial earthquake and a maximum slip duration at each source element of 20 s and a total source duration of 20 s for the second earthquake (Figure 2). We represent potency-rate functions as a set of linear B splines (multi-time window), and we adopted sufficiently long durations so that each source element can flexibly represent possible multiple slip episodes as data requires. As we will present later, our key finding of apparent back-rupture propagation is robustly resolved against the different assumptions of maximum slip duration at each source element (Figure S10 in Supporting Information S1).

Our modeling strategy shares a similarity with that of seismic back-projection, which requires very few assumptions about the fault geometry and rupture information (Ishii et al., 2005; Meng et al., 2012; Nissen et al., 2016; Satriano et al., 2012; Taymaz et al., 2021; Y. Xu et al., 2009; Yao et al., 2011). Our approach additionally provides kinematic information by directly solving for the potency-rate density distribution, which should enable in-depth evaluation of rupture dynamics that, for example, can be associated with variable fault geometry. To perform a stable inversion with such a high degree-of-freedom model without overfitting, the uncertainty of the Green's function is incorporated into the data covariance matrix (Yagi & Fukahata, 2011) and the strength of smoothing is adjusted using the Akaike's Bayesian Information Criterion (e.g., Akaike, 1980; Sato et al., 2022; Yabuki & Matsu'ura, 1992). We note the effect of structural heterogeneity can also be translated into the uncertainty of Green's functions if it is stochastic, yet it still impacts the finite-fault solution given the complex tectonic setting in the study region, which may affect the relative timing of rupture. As demonstrated in Figure S9 in Supporting Information S1, allowing a high degree of freedom of modeling should rather help stabilize the solution; for example, only allowing pure vertical strike-slip faulting yields poor data fits (Figure S9 in Supporting Information S1) and an unstable solution that yields an opposite sense-of-slip to what is expected for the regional tectonic regime (e.g., Fukahata & Wright, 2008). This exercise highlights the importance of permitting a complex rupture scenario with enough model freedom and over-constraining the model would fail to explain the seismic signals that are responsible for the change of focal mechanism during rupture (e.g., Shimizu et al., 2020). Aftershock focal mechanisms and moment tensors show a variability with a deviation from pure strike-slip faulting (Figure 1), helping to demonstrate that a flexible potency-density tensor approach is required.

We applied a standardized data processing workflow for our potency-density tensor approach that has been applied to earthquakes in different tectonic regimes (Fan et al., 2022; Fang et al., 2022; Hicks et al., 2020; Hu et al., 2021; Shimizu et al., 2020; Tadapansawut et al., 2021; Yagi et al., 2023; Yamashita, Yagi, Okuwaki, Shimizu, et al., 2022). We used the vertical component of teleseismic *P*-waveforms from a total of 39 and 37 stations for the M_W 7.9 and M_W 7.6 earthquakes, respectively (Figures S1 and S2 in Supporting Information S1). The data were selected to ensure sufficient azimuthal coverage so that we can resolve potential variations of radiation pattern during the rupture evolution and hence spatiotemporal changes of fault geometry. We selected data so that we manually picked the first motion of *P*-wave (e.g., Okuwaki et al., 2016). The data were then restituted to velocity at 1.0-s sampling interval by removing the instrumental responses. Green's functions were calculated based on the method of Kikuchi and Kanamori (1991), adopting CRUST1.0 model (Laske et al., 2013) for the one-dimensional layered velocity structure around the source region (Table S1 in Supporting Information S1). We further tested the robustness of our modeling against an alternative structural model adopted from the ak135 model (Kennett et al., 1995) (Table S2 in Supporting Information S1), showing that the resultant pattern of potency-density tensors is less sensitive to the choice of the near-source structure model (Figure S7 in Supporting Information S1). The initial rupture point is taken from the relocated epicenter for the M_W 7.9 earthquake (Melgar et al., 2023) and on the model fault near the relocated epicenter for the M_W 7.6 earthquake. We set the hypocentral depth at 15 km for both earthquakes (Figure S3 in Supporting Information S1). The uniformly-distributed model source elements are regularly spaced 10×5 km and 5×5 km in the along-strike and dip directions for the M_W 7.9 and M_W 7.6 earthquakes, respectively, along a vertically dipping non-planar model fault that aligns with the active faults (Emre et al., 2018) and the relocated aftershocks (Figure S3 in Supporting Information S1). Together with the curved main EAF strand, we adopted a splay fault into our model fault centered on the initial rupture point, which is oriented at 35° NE, having an acute angle relative to the main EAF in NE direction (Figure S3 in Supporting Information S1).

3. Results

3.1. Initial M_W 7.9 Nurdağı-Pazarcık Earthquake

Our potency-density tensor inversion finds the first earthquake ruptured a total of 350 km length; 200 km length northeast from the epicenter and 150 km southwest of the epicenter along our modeled fault, including the splay fault domain (Figure 2 and Figure S4 in Supporting Information S1). The total seismic moment is 9.6×10^{20} N m (M_W 7.9), which is similar to the that estimated from coda waves (X. Jiang et al., 2023). The overall faulting mechanism indicated by the flexible potency density tensors is consistent with our prescribed non-planar model fault geometry (Figure 2). The potency-density tensors show a largely planar fault with depth. The space-time evolution of the rupture shows four distinct episodes which we describe in the following paragraphs.

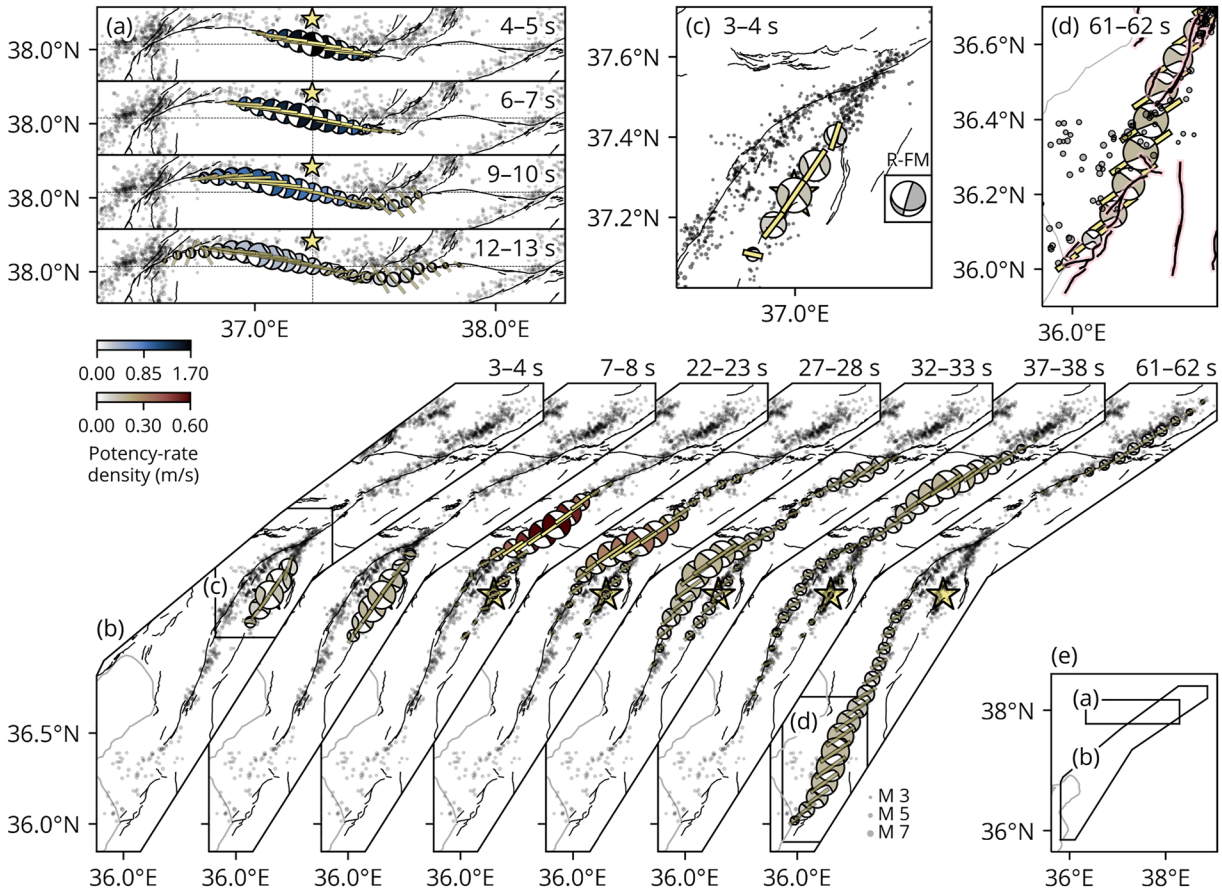

Figure 3. Selected snapshots of the spatiotemporal potency-rate density tensor distributions for (a) the M_W 7.6 and (b) M_W 7.9 earthquakes. The time window for the snapshot is shown on the corresponding panel. The yellow bar is the strike orientation extracted from the best-fitting double-couple components of the resultant potency-rate density tensors. The size of the beachball is scaled by the maximum potency-rate density in the corresponding time window. The optimum strike angle is one of the two possible nodal planes that minimizes the inner product of fault-normal vectors of the candidate plane and the reference fault plane: 54°/90° and 261°/90° (strike/dip) for the M_W 7.9 and the M_W 7.6 earthquakes, respectively. Only the source elements of the maximum potency-rate density along depth are shown. The full snapshots are shown in Movies S1–S3. Panels (c, d) show the enlarged view of the initial and fourth rupture episodes, respectively. The inset on (c) shows the best-fitting focal mechanism: 197°/86°/56° (strike/dip/rake) determined by first-motions recorded by seismometer and strong-motion stations up to 350 km away (see Data Availability Statement) using the method of Hardebeck and Shearer (2002) with takeoff angles computed in the velocity model of Melgar et al. (2020). The stars, dots, and lines are the same as shown in Figure 1. Panel (e) shows the map extents of (a, b).

Rupture Episode 1. The first-motion faulting mechanism using local-regional waveforms (Figure 3) indicates this rupture initiated at the hypocenter along a fault plane with a NE-SW fault, but with an oblique-normal sense of slip after nucleation, the rupture then propagates bilaterally toward the NE and SW for the first 10 s after origin time, extending 25 km either side of the hypocenter along the splay fault. The moment-rate release of this initial rupture episode is minor, having only 3% of the total seismic moment (M_W 6.9). Our potency-rate density tensor solution shows left-lateral faulting on a faulting striking 36° (based on the largest potency rate in 7–8 s time window; Figure 3), more consistent with the prescribed splay fault rather than the main EAF (Figure 3).

Rupture Episode 2. After a relative quiescence for 5 s after the end of the first episode, the second rupture episode starts at OT+15 s, lying 60 km NE of the epicenter. This episode releases the greatest amount of seismic moment (35%; M_W 7.6) of the entire rupture. The rupture propagates in an asymmetric bilateral manner with a strong SW-oriented direction, rupturing a total length of 120 km over 20 s duration. Most notably, the SW flank of the rupture front apparently back-propagates through the hypocentral region beyond 20 km SW of the epicenter (Figure 2). The migration speed of the associated SW-directing back-propagating rupture signal exceeds the local *S*-wave velocity (Table S1 in Supporting Information S1; Laske et al., 2013) (Figure 2; Movies S1 and S2), indicating super-shear rupture during the latter portion of this rupture episode. Although rigorous estimates of rupture velocity can be limited due to the smoothing constraints, the migration speed of this high slip-rate zone

is related to the rupture-front velocity (Okuwaki et al., 2020), and has been calibrated well with rupture velocities from independent back-projection results for other earthquakes (e.g., Hicks et al., 2020). The fault geometry estimated from our potency-density tensor approach shows vertical strike-slip faulting with a strike of 55° (e.g., where we solved the largest potency rate at 22–23 s; Figure 3) that is consistent with the main EAF. We note that the source elements with minor potency rate may be affected by the surrounding major potency rate due to smoothing effects, so we do not interpret the resultant strike angle from those minor potency-rate tensors.

Rupture Episode 3. A third rupture phase NE of the hypocenter begins to be dominant from OT+35 s, soon after the SW back-rupture propagation decays. This phase accounts for 15% of the total seismic moment (M_W 7.4). It first propagates to the SW near the NE flank of the second rupture episode, but then the NE-oriented component of the bilateral rupture becomes more dominant during OT+37–45 s, rupturing a total length of 100 km until it immediately stops near the NE edge of the model domain at 120 km NE from the epicenter (Figure 2). The strike orientation is similar to that of Episode 2 and remains consistent with the main EAF. We refrain from measuring rupture speeds for this episode as they seem sensitive to the assumption of maximum slip duration (Figure S10 in Supporting Information S1).

Rupture Episode 4. A fourth rupture episode starts at OT+45 s in the SW corner of the model domain, partially overlapping in space with the second rupture. The rupture front unilaterally propagates toward the SW at fast, supershear speed, exceeding the local *S*-wave velocity during OT+45–55 s. Then, the rupture front apparently slows down ∼150 km SW of the junction between the EAF and splay faults, and completely stops at 75 s. The strike orientation is 54° (based on the largest potency rate in 50–51 s time window). The fourth rupture episode has 43% of the total seismic moment (M_W 7.7), and the potency-density tensors have a median non-double couple component of 24% (e.g., 60–61 s; Figure 3).

3.2. Secondary M_W 7.6 Ekinözü Earthquake

The rupture of the later M_W 7.6 earthquake is much more confined, rupturing 80 km length and 20 km width over a single episode, and the total seismic moment is 3.2×10^{20} N m (M_W 7.6). The rupture evolution is asymmetric bilateral with a dominant westwards-directed rupture from the epicenter. The west-oriented rupture propagates at faster than the local *S*-wave velocity (Table S1 in Supporting Information S1; Figure 2; Movies S1 and S3) from 6 to 10 s. The rupture immediately stops at around 15 s. The fault geometry estimated from our potency-density tensors has an EW-oriented curved fault strike with strike-slip faulting, which is well aligned with the prescribed curved model plane geometry. The estimated fault dip is dominantly vertical, but the dip angle slightly shallows with depth from 76° to 61°, as defined by the maximum along-strike potency density (Figure S4b in Supporting Information S1). Near the end of the rupture, dip-slip faulting components become dominant at the tips of the main rupture, with strikes rotated north-south (Figure 3).

4. Discussion

4.1. M_W 7.9 Event: Rupture Initiation on a Splay Fault to the Main EAF

The initial rupture of the M_W 7.9 event has a different fault orientation than that of the following main bilateral rupture that releases most (97%) of the seismic moment. For example, during the peak slip of the first rupture episode (7–8 s), the strike is 36°, whilst the later bilateral rupture episode has a strike of 55° (Figure 3). Intense aftershock activity is observed NE of the epicenter (Melgar et al., 2023), in a lineation oriented SW to NE, seemingly connecting to the main EAF strand (Figure 3). The alignment of these aftershocks on the splay fault is consistent with the strike estimated from our inversion. To the east of the epicenter, the Narlıdağ fault zone has been mapped to extend to the N and NE (Duman & Emre, 2013; Perinçek & Çemen, 1990). From rapid analyses of the satellite images and field measurements, surface rupture is also observed near the epicenter, which is elongated NE and is consistent with our estimated strike orientation (Reitman et al., 2023), which is called as Nurdağı-Pazarcık fault by Melgar et al. (2023). Thus, the first rupture episode occurred on a sub-parallel splay fault to the main EAF. Although our potency-density tensor inversion finds mostly pure strike-slip faulting during the first rupture episode, the first-motion mechanism from near-field waveforms suggest that the rupture initiated with a weak phase of oblique-normal faulting (Figure 3c), which is likely too small to be resolved in teleseismic waveforms. From our estimated strike orientations, the angle between the splay fault and the main EAF model domain is ∼18°, which is close to the peak of the splay fault angle distributions (±17°) that was previously

observed for active faults in California (Ando et al., 2009; Scholz et al., 2010). In between the first and second rupture episodes, we only see minor moment release, which may suggest a non-continuous rupture at the junction between the splay fault and main EAF. However, due to the insufficient spatial resolution of the teleseismic data we used, it is difficult to rigorously discuss how the splay fault and the main EAF are physically connected solely based on our result.

4.2. Rupture Dynamics During Apparent Back-Propagating Slip

One of the most notable features of the M_W 7.9 earthquake is the asymmetric bilateral rupture of the second episode during OT+15–35 s (Figure 2), where the SW flank of the bilateral rupture apparently propagates back through the hypocentral area. We confirmed this apparent back-propagation rupture behavior is robustly retrieved even if we changed model assumptions, such as the maximum duration of bases slip functions and the hypothesized rupture-front speed (Figures S10 and S11 in Supporting Information S1). Such a boomerang-like back rupture propagation is an end-member rupture behavior that has become more frequently reported with higher-resolution datasets and more detailed rupture imaging (Hicks et al., 2020; Meng et al., 2014; Vallée et al., 2023; Yamashita, Yagi, & Okuwaki, 2022). However, because the earthquakes in all of these cases studied were either deep or in remote areas, there were no surface rupture observations that could have explained the apparent back-rupture propagation. Therefore, the apparent boomerang rupture of the 2023 SE Türkiye earthquake is intriguing because we show that the rupture propagated along different sub-parallel fault strands which could offer an mechanism for these previously reported examples of back-propagating ruptures.

Although it is still difficult to find a deterministic explanation of why the initial rupture occurred on the more minor bifurcated fault rather than the main EAF, the series of multiple ruptures that are responsible for the resultant boomerang-like rupture can be explained by a cascading up of rupture size based on a hierarchical rupture model (e.g., Ide & Aochi, 2005; Otsuki & Dilov, 2005). In this case, the main rupture could have been dynamically triggered by the initial splay fault rupture as it cascades up to the longer scale of the rupture. The main EAF should have accumulated enough strain due to the plate accommodation (e.g., Aktug et al., 2016; Weiss et al., 2020), which makes it ready to be ruptured once assisted by the initial rupture on the bifurcated fault. Although our sole use of teleseismic data may not rigorously discriminate the absolute location of the slip on the closely located parallel faults, we favor that the apparent back-propagating part of the rupture occurred on the main EAF because of the higher potency rate on the main EAF model fault rather than on the splay model fault (Figures 2c and 2d). This assumption is supported by independent modeling using geodetic datasets that finds larger slip along the main EAF than on the splay fault (Barbot et al., 2023; Mai et al., 2023; Melgar et al., 2023).

Rupture dynamics across branching faults have been extensively studied by numerical simulations (Ando & Yamashita, 2007; Aochi et al., 2000; Bhat et al., 2007; Kame et al., 2003; Okubo et al., 2020; S. Xu et al., 2015). Backward branching rupture is particularly proposed (Fliss et al., 2005), where stress accumulation at the tip of the main fault enhances rupture jump onto the neighboring branch fault, nucleating bilateral rupture in which one flank can be seen as apparent backward rupture. Although it remains to be solved whether the initial rupture is physically intersecting the main EAF or not, our source model shows that the initial rupture is not continuously propagating with a sufficiently strong slip-rate into the main EAF, and the second rupture episode begins on the main EAF ~20 km SW from the apparent junction of the initial fault strand and the main EAF. The spatiotemporal gap between the initial and second rupture episodes might play a role to enable the cascade up or jump of rupture to the larger scale main rupture. The main EAF west of the junction with the Narlıdağ fault zone should be situated in the extensional quadrant of the left-lateral Rupture Episode 1, which may impart a stress shadow on the main EAF. Such a stress shadow may have disrupted the SW-directed Rupture Episode 2, which we see as a temporary rupture deceleration at OT+15–20 s before it then accelerated to a discrete phase of supershear rupture (Figure 2). The rupture propagation toward SW through the hypocentral region may be enabled because the longer-scale main EAF rupture should have enough fracture energy to easily overcome the area affected by the stress shadow possibly generated by the lower level of rupture episode. Dynamic rupture simulations will help to shed further light on rupture processes across this fault junction (e.g., Rosakis et al., 2023).

The strike orientation during the second rupture episode (OT+15–20 s) is slightly rotated clockwise, which is also mapped in the main EAF strand west of the junction (Figures 1 and 3). If this change in fault orientation acts as a restraining bend given the background stress field, the rupture propagation may cause a concentration of stress at the bend. This might have caused the rupture deceleration, which can be seen as the slip stagnation

during OT+15–20 s. Soon after this pause, dynamic stresses allowed the rupture to continue and propagate to the SW and even briefly accelerate its speed, which can be consistent with the predicted behavior of a supershear rupture transition across restraining bends (e.g., Bruhat et al., 2016). We emphasize here that our source model does show that the *M*w 7.9 earthquake is not supershear throughout the entire event, but it involves discrete supershear along certain fault segments during each rupture episode. Such discrete supershear pulses have been independently estimated using near-field records (e.g., Delouis et al., 2023) and numerical simulations (e.g., Abdelmeguid et al., 2023).

We further note that the NE and SW boundaries of the second rupture episode coincide with mapped fault steps near Gölbaşı and south of Nurdağı (see locations S1 and S2 in Figure S5 in Supporting Information S1). Such steps may contribute to the apparent gaps of 10 s between the second and subsequent rupture episodes (Figure S5 in Supporting Information S1). We do not have enough evidence to explain how such gaps are physically connected, but our finding will stimulate further research to investigate how the rupture evolved across fault steps, for example, the long nucleation processes or possibly inter-subevent slow deformation.

4.3. The SW-End Third Rupture Episode Broke Multiple Fault Segments

Together with the radiation pattern of left-lateral faulting, the strong directivity of the SW-oriented back rupture process can result in a further cascading of the rupture toward the SW. Our source model exhibits a relatively fast and smooth rupture along the section near Nurdağı, whilst it suddenly slows down at 55 s, where the rupture intersects at the apparent left-step in the active fault strand south of Hassa (Figure 1). Although the SW-oriented rupture propagation and the deceleration of migration speed south of Hassa are robustly resolved, we refrain from discussing the potency rate found at the very beginning of the rupture episode 4 (at around ∼0 km from the fault junction; Figure 2c) because it is located close to the model boundary and its appearance is dependent on the assumption of duration of potency-rate functions (Figure S10 in Supporting Information S1).

The strike extracted from the best-double-couple solution of our estimated potency-density tensors is not apparently aligned with the bulk linear trend of the active faults (Figure 2). However, because we observe non-double-couple fractions for the SW end rupture (e.g., 24% during 60–61 s; Figure 3), we cannot clearly define which individual fault strands likely ruptured. South of Hassa, several distinct fault segments are separated by step-overs (Figure 3) (Duman & Emre, 2013). The aftershock distribution here is also more scattered than elsewhere along the main EAF and along the splay fault. These aftershock patterns appear consistent between catalogs using different relocation methods (Lomax, 2023; Melgar et al., 2023) (Figure S8 in Supporting Information S1); however, we cannot rule out a greater earthquake location uncertainty due to diminished regional seismic network coverage close to the Syria border. Pre-earthquake field measurements (Duman & Emre, 2013; Emre et al., 2018), as well as the fault rupture mapping immediately after the 2023 earthquakes (Reitman et al., 2023) show a zigzag geometry involving the bends and curves. This evidence collectively suggests that the later phase of rupture may have involved multiple faults with different geometries in the SW.

4.4. M_W 7.6 Event: Curved and Focused Rupture

We find the M_W 7.6 earthquake shows a much more focused rupture process, compared with the preceding M_W 7.9 event. Yet, our solution finds that the strike of the ruptured fault geometry curves gradually, with a counterclockwise rotation toward the west. The rotation trend can favorably be oriented to the optimal plane of the background horizontal stress given the bulk E-W oriented left-lateral strike-slip system of the Sürgü fault zone. This trend can thus favor rupture propagation, in a similar way to a fault-releasing bend (e.g., Kase & Day, 2006). In addition, such a favorably curved fault geometry may have facilitated the supershear rupture (e.g., Bruhat et al., 2016; Trugman & Dunham, 2014), albeit over a relatively short distance. At the western and eastern ends of the model domain, we find a significant change of mapped fault geometry and the orientation of the potency density tensors. At these domains, the strike orientation is almost NS, and dip-slip faulting becomes dominant. The complex network in Göksun-Savrun faults to the west and Nurhak Fault complex to the east (Duman & Emre, 2013) can explain such the significant change of fault geometry, asymmetric nature of the bilateral rupture, and the likely reason for abrupt rupture termination at both ends.

The collocation of the two M_W 7.9 and M_W 7.6 earthquakes, only separated around 9 hr apart, may give rise to a question over how the initial M_W 7.9 earthquake can affect and possibly trigger the later M_W 7.6 earthquake. Such

earthquake doublets have been reported before in different tectonic environments (e.g., Ammon et al., 2008; Astiz & Kanamori, 1984; Fan et al., 2016; Hicks & Rietbrock, 2015; Y. Jiang et al., 2022; Lay & Kanamori, 1980; Lay et al., 2013; Nissen et al., 2016; Ross et al., 2019; ten Brink et al., 2020; Yagi et al., 2023). Our Coulomb stress analyses using our estimated source model shows the M_W 7.9 earthquake may have induced positive static stress change in the hypothesized M_W 7.6 source domain (~0.4 bar) (Figure S6 in Supporting Information S1), which may have brought the fault that hosted the M_W 7.6 earthquake closer to failure.

5. Conclusions

We find the differently oriented, curved, and multiple fault segments facilitate the series of complex rupture geometries during the devastating earthquakes in 2023. Back-propagating rupture with discrete interludes of rupture at supershear velocity during the initial M_W 7.9 earthquake was facilitated by the branching fault rupture that provided an initial stress trigger to the larger-scale main EAF rupture. The secondary M_W 7.6 earthquake involved a more continuous, westward-directed supershear rupture, which was abruptly interrupted by the geometric barriers in both the western and eastern ends of the northern strand of the EAF, being responsible for the relatively focused rupture extent. Our results suggest the geometrically complex fault network around the source region should be key to developing multi-scale cascading rupture growth and alternating rupture directions, which will be critical inputs for both our understanding of earthquake source physics and better assessment of the future damaging earthquakes in complex fault zones.

Data Availability Statement

Materials presented in this paper are archived and available at https://doi.org/10.5281/zenodo.7678181. The seismic data were downloaded through the IRIS Wilber 3 system (https://ds.iris.edu/wilber3/find_event) or IRIS Web Services (https://service.iris.edu). We used ObsPy (https://doi.org/10.5281/zenodo.165135; Beyreuther et al., 2010), Pyrocko (https://pyrocko.org/; Heimann et al., 2017), matplotlib (https://doi.org/10.5281/zenodo.592536; Hunter, 2007), Cartopy (https://doi.org/10.5281/zenodo.1182735; Met Office, 2015; Elson et al., 2022), Generic Mapping Tools (https://doi.org/10.5281/zenodo.3407865; Wessel & Luis, 2017); and Scientific color maps (https://doi.org/10.5281/zenodo.1243862; Crameri, 2018; Crameri et al., 2020) for data processing and visualization. First motion mechanisms were picked using waveform data from the following seismic networks: KO (https://doi.org/10.7914/SN/KO); IM (https://www.fdsn.org/networks/detail/IM/); TK (https://doi.org/10.7914/SN/TK); and TU (https://doi.org/10.7914/SN/TU).

Acknowledgments
We thank the editor Germán Prieto and the reviewer Erdinc Saygin and the anonymous reviewer for their thorough evaluations and providing constructive comments and suggestions. We also thank Ahmed Ettaf Elbanna, František Gallovič, and Jiří Zahradník for fruitful discussion. The facilities of IRIS Data Services, and specifically the IRIS Data Management Center, were used for access to waveforms, related metadata, and/or derived products used in this study. IRIS Data Services are funded through the Seismological Facilities for the Advancement of Geoscience (SAGE) Award of the National Science Foundation under Cooperative Support Agreement EAR-1851048. We appreciate the Disaster and Emergency Management Presidency of Türkiye (AFAD) for providing an initial catalogue of aftershocks and phase-arrival data acquired from their bulletin resources. This work was supported by JSPS Grant-in-Aid for Scientific Research (C) 19K04030 and 22K03751, JSPS Early-Career Scientists 20K14570, and JSPS Grant-in-Aid for Special Purposes 22K21372. The authors declare no conflicts of interest relevant to this study.

References

Abdelmeguid, M., Zhao, C., Yalcinkaya, E., Gazetas, G., Elbanna, A., & Rosakis, A. J. (2023). Revealing the dynamics of the February 6th 2023 M 7.8 Kahramanmaraş/Pazarcik earthquake: Near-field records and dynamic rupture. *EarthArXiv*. https://doi.org/10.31223/X5066R

Abercrombie, R. E., Antolik, M., & Ekström, G. (2003). The June 2000 *M*w 7.9 earthquakes south of Sumatra: Deformation in the India-Australia plate. *Journal of Geophysical Research*, *108*(B1), ESE6-1–ESE6-16. https://doi.org/10.1029/2001jb000674

AFAD. (2023). AFAD (disaster and emergency management presidency) earthquake catalog. Retrieved from https://deprem.afad.gov.tr/event-catalog

AFAD Focal Mechanism Solution. (2023). AFAD focal mechanism solution. Retrieved from https://deprem.afad.gov.tr/event-focal-mechanism

Akaike, H. (1980). Likelihood and the Bayes procedure. *Trabajos de Estadistica y de Investigacion Operativa*, *31*(1), 143–166. https://doi.org/10.1007/BF02888350

Aktug, B., Ozener, H., Dogru, A., Sabuncu, A., Turgut, B., Halicioglu, K., et al. (2016). Slip rates and seismic potential on the East Anatolian Fault System using an improved GPS velocity field. *Journal of Geodynamics*, *94–95*, 1–12. https://doi.org/10.1016/j.jog.2016.01.001

Ambraseys, N. N. (1989). Temporary seismic quiescence: SE Turkey. *Geophysical Journal International*, *96*(2), 311–331. https://doi.org/10.1111/j.1365-246X.1989.tb04453.x

Ambraseys, N. N., & Jackson, J. A. (1998). Faulting associated with historical and recent earthquakes in the Eastern Mediterranean region. *Geophysical Journal International*, *133*(2), 390–406. https://doi.org/10.1046/j.1365-246X.1998.00508.x

Ammon, C. J., Kanamori, H., & Lay, T. (2008). A great earthquake doublet and seismic stress transfer cycle in the central Kuril Islands. *Nature*, *451*(7178), 561–565. https://doi.org/10.1038/nature06521

Ando, R., Shaw, B. E., & Scholz, C. H. (2009). Quantifying natural fault geometry: Statistics of splay fault angles. *Bulletin of the Seismological Society of America*, *99*(1), 389–395. https://doi.org/10.1785/0120080942

Ando, R., & Yamashita, T. (2007). Effects of mesoscopic-scale fault structure on dynamic earthquake ruptures: Dynamic formation of geometrical complexity of earthquake faults. *Journal of Geophysical Research*, *112*(9), 1–15. https://doi.org/10.1029/2006JB004612

Aochi, H., Fukuyama, E., & Matsu'ura, M. (2000). Selectivity of spontaneous rupture propagation on a branched fault. *Geophysical Research Letters*, *27*(22), 3635–3638. https://doi.org/10.1029/2000GL011560

Arpat, E., & Saroglu, F. (1972). The East Anatolian fault system; thoughts on its development. *Mineral Research and Exploration Institute of Turkey*, *78*, 33–39. Retrieved from https://dergipark.org.tr/en/pub/bulletinofmre/issue/3904/52066

Astiz, L., & Kanamori, H. (1984). An earthquake doublet in Ometepec, Guerrero, Mexico. *Physics of the Earth and Planetary Interiors*, *34*(1–2), 24–45. https://doi.org/10.1016/0031-9201(84)90082-7

Bao, H., Ampuero, J.-P., Meng, L., Fielding, E. J., Liang, C., Milliner, C. W. D., et al. (2019). Early and persistent supershear rupture of the 2018 magnitude 7.5 Palu earthquake. *Nature Geoscience*, *12*(3), 200–205. https://doi.org/10.1038/s41561-018-0297-z

Barbot, S., Luo, H., Wang, T., Hamiel, Y., Piatibratova, O., Javed, M. T., et al. (2023). Slip distribution of the February 6, 2023 *M*w 7.8 and *M*w 7.6, Kahramanmaraş, Turkey earthquake sequence in the East Anatolian Fault Zone. *Seismica*, *2*(3). https://doi.org/10.26443/seismica.v2i3.502

Beyreuther, M., Barsch, R., Krischer, L., Megies, T., Behr, Y., & Wassermann, J. (2010). ObsPy: A python toolbox for seismology. *Seismological Research Letters*, *81*(3), 530–533. https://doi.org/10.1785/gssrl.81.3.530

Bhat, H. S., Olives, M., Dmowska, R., & Rice, J. R. (2007). Role of fault branches in earthquake rupture dynamics. *Journal of Geophysical Research*, *112*(B11), B11309. https://doi.org/10.1029/2007JB005027

Bird, P. (2003). An updated digital model of plate boundaries. *Geochemistry, Geophysics, Geosystems*, *4*(3), 1105. https://doi.org/10.1029/2001GC000252

Bruhat, L., Fang, Z., & Dunham, E. M. (2016). Rupture complexity and the supershear transition on rough faults. *Journal of Geophysical Research: Solid Earth*, *121*(1), 210–224. https://doi.org/10.1002/2015JB012512

Crameri, F. (2018). Geodynamic diagnostics, scientific visualisation and StagLab 3.0. *Geoscientific Model Development*, *11*(6), 2541–2562. https://doi.org/10.5194/gmd-11-2541-2018

Crameri, F., Shephard, G. E., & Heron, P. J. (2020). The misuse of colour in science communication. *Nature Communications*, *11*(1), 5444. https://doi.org/10.1038/s41467-020-19160-7

Dal Zilio, L., & Ampuero, J.-p. (2023). Earthquake doublet in Turkey and Syria. *Communications Earth & Environment*, *4*(1), 71. https://doi.org/10.1038/s43247-023-00747-z

Das, S., & Aki, K. (1977). Fault plane with barriers: A versatile earthquake model. *Journal of Geophysical Research*, *82*(36), 5658–5670. https://doi.org/10.1029/JB082i036p05658

Delouis, B., van den Ende, M., & Ampuero, J.-P. (2023). Kinematic rupture model of the February 6th 2023 *M*w7.8 Turkey earthquake from a large set of near-source strong motion records combined by GNSS offsets reveals intermittent supershear rupture. *ESS Open Arch*. https://doi.org/10.22541/essoar.168286647.71550161/v1

Duman, T. Y., Elmacı, H., Özalp, S., Kürçer, A., Kara, M., Özdemir, E., et al. (2020). Paleoseismology of the western Sürgü-Misis fault system: East Anatolian Fault, Turkey. *Mediterranean Geoscience Reviews*, *2*(3), 411–437. https://doi.org/10.1007/s42990-020-00041-6

Duman, T. Y., & Emre, Ö. (2013). The East Anatolian Fault: Geometry, segmentation and jog characteristics. *Geological Society, London, Special Publications*, *372*(1), 495–529. https://doi.org/10.1144/SP372.14

Dziewonski, A. M., Chou, T.-A., & Woodhouse, J. H. (1981). Determination of earthquake source parameters from waveform data for studies of global and regional seismicity. *Journal of Geophysical Research*, *86*(B4), 2825–2852. https://doi.org/10.1029/JB086iB04p02825

Ekström, G., Nettles, M., & Dziewoński, A. (2012). The global CMT project 2004–2010: Centroid-moment tensors for 13,017 earthquakes. *Physics of the Earth and Planetary Interiors*, *200–201*, 1–9. https://doi.org/10.1016/j.pepi.2012.04.002

Elson, P., de Andrade, E. S., Lucas, G., May, R., Hattersley, R., Campbell, E., et al. (2022). Scitools/cartopy: v0.21.1. *Zenodo*. https://doi.org/10.5281/zenodo.7430317

Emre, Ö., Duman, T. Y., Özalp, S., ÅžaroÄŸlu, F., Olgun, Å., Elmacı, H., & Çan, T. (2018). Active fault database of Turkey. *Bulletin of Earthquake Engineering*, *16*(8), 3229–3275. https://doi.org/10.1007/s10518-016-0041-2

Fan, W., Okuwaki, R., Barbour, A. J., Huang, Y., Lin, G., & Cochran, E. S. (2022). Fast rupture of the 2009 *M*w 6.9 Canal de Ballenas earthquake in the Gulf of California dynamically triggers seismicity in California. *Geophysical Journal International*, *230*(1), 528–541. https://doi.org/10.1093/gji/ggac059

Fan, W., Shearer, P. M., Ji, C., & Bassett, D. (2016). Multiple branching rupture of the 2009 Tonga-Samoa earthquake. *Journal of Geophysical Research: Solid Earth*, *121*(8), 5809–5827. https://doi.org/10.1002/2016JB012945

Fang, J., Ou, Q., Wright, T. J., Okuwaki, R., Amey, R. M. J., Craig, T. J., et al. (2022). Earthquake cycle deformation associated with the 2021 *M*w 7.4 Maduo (Eastern Tibet) earthquake: An intrablock rupture event on a slow-slipping fault from Sentinel-1 InSAR and teleseismic data. *Journal of Geophysical Research: Solid Earth*, *127*(11), e2022JB024268. https://doi.org/10.1029/2022JB024268

Fliss, S., Bhat, H. S., Dmowska, R., & Rice, J. R. (2005). Fault branching and rupture directivity. *Journal of Geophysical Research*, *110*(B6), B06312. https://doi.org/10.1029/2004JB003368

Fukahata, Y., & Wright, T. J. (2008). A non-linear geodetic data inversion using ABIC for slip distribution on a fault with an unknown dip angle. *Geophysical Journal International*, *173*(2), 353–364. https://doi.org/10.1111/j.1365-246X.2007.03713.x

Gallovič, F., Zahradník, J., Plicka, V., Sokos, E., Evangelidis, C., Fountoulakis, I., & Turhan, F. (2020). Complex rupture dynamics on an immature fault during the 2020 *M*w 6.8 Elazığ earthquake, Turkey. *Communication Earth & Environment*, *1*(1), 40. https://doi.org/10.1038/s43247-020-00038-x

Hall, S. (2023). What Turkey's earthquake tells us about the science of seismic forecasting. *Nature*, *615*(7952), 388–389. https://doi.org/10.1038/d41586-023-00685-y

Hardebeck, J. L., & Shearer, P. M. (2002). A new method for determining first-motion focal mechanisms. *Bulletin of the Seismological Society of America*, *92*(6), 2264–2276. https://doi.org/10.1785/0120010200

Hartzell, S. H., & Heaton, T. H. (1983). Inversion of strong ground motion and teleseismic waveform data for the fault rupture history of the 1979 Imperial Valley, California, earthquake. *Bulletin of the Seismological Society of America*, *73*(6A), 1553–1583. https://doi.org/10.1785/BSSA07306A1553

Heimann, S., Kriegerowski, M., Isken, M., Cesca, S., Daout, S., Grigoli, F., et al. (2017). *Pyrocko—An open-source seismology toolbox and library*. GFZ Data Services. https://doi.org/10.5880/GFZ.2.1.2017.001

Hicks, S. P., Okuwaki, R., Steinberg, A., Rychert, C. A., Harmon, N., Abercrombie, R. E., et al. (2020). Back-propagating supershear rupture in the 2016 *M*w 7.1 Romanche transform fault earthquake. *Nature Geoscience*, *13*(9), 647–653. https://doi.org/10.1038/s41561-020-0619-9

Hicks, S. P., & Rietbrock, A. (2015). Seismic slip on an upper-plate normal fault during a large subduction megathrust rupture. *Nature Geoscience*, *8*(12), 955–960. https://doi.org/10.1038/ngeo2585

Hu, Y., Yagi, Y., Okuwaki, R., & Shimizu, K. (2021). Back-propagating rupture evolution within a curved slab during the 2019 *M*w 8.0 Peru intraslab earthquake. *Geophysical Journal International*, *227*(3), 1602–1611. https://doi.org/10.1093/gji/ggab303

Huang, Y. (2018). Earthquake rupture in fault zones with along-strike material heterogeneity. *Journal of Geophysical Research: Solid Earth*, *123*(11), 9884–9898. https://doi.org/10.1029/2018JB016354

Hunter, J. D. (2007). Matplotlib: A 2D graphics environment. *Computer Science and Engineering*, *9*(3), 90–95. https://doi.org/10.1109/MCSE.2007.55

Hussain, E., Kalaycıoğlu, S., Milliner, C. W. D., & Çakir, Z. (2023). Preconditioning the 2023 Kahramanmaraş (Türkiye) earthquake disaster. *Nature Reviews Earth & Environment*, *4*, 5–7. https://doi.org/10.1038/s43017-023-00411-2

Ide, S., & Aochi, H. (2005). Earthquakes as multiscale dynamic ruptures with heterogeneous fracture surface energy. *Journal of Geophysical Research*, *110*(B11), 1–10. https://doi.org/10.1029/2004JB003591

Ishii, M., Shearer, P. M., Houston, H., & Vidale, J. E. (2005). Extent, duration and speed of the 2004 Sumatra-Andaman earthquake imaged by the Hi-Net array. *Nature*, *435*(7044), 933–936. https://doi.org/10.1038/nature03675

Jackson, J., & McKenzie, D. (1984). Active tectonics of the Alpine–Himalayan Belt between western Turkey and Pakistan. *Geophysical Journal International*, *77*(1), 185–264. https://doi.org/10.1111/j.1365-246X.1984.tb01931.x

Jiang, X., Song, X., Li, T., & Wu, K. (2023). Moment magnitudes of two large Turkish earthquakes in February 2023 from long-period coda. *KeAi Earthquake Science*. https://doi.org/10.2139/ssrn.4361747

Jiang, Y., González, P. J., & Bürgmann, R. (2022). Subduction earthquakes controlled by incoming plate geometry: The 2020 M > 7.5 Shumagin, Alaska, earthquake doublet. *Earth and Planetary Science Letters*, *584*, 117447. https://doi.org/10.1016/j.epsl.2022.117447

Kame, N., Rice, J. R., & Dmowska, R. (2003). Effects of prestress state and rupture velocity on dynamic fault branching. *Journal of Geophysical Research*, *108*(B5), 1–21. https://doi.org/10.1029/2002JB002189

Kase, Y., & Day, S. M. (2006). Spontaneous rupture processes on a bending fault. *Geophysical Research Letters*, *33*(10), 1–4. https://doi.org/10.1029/2006GL025870

Kennett, B. L., Engdahl, E. R., & Buland, R. (1995). Constraints on seismic velocities in the Earth from traveltimes. *Geophysical Journal International*, *122*(1), 108–124. https://doi.org/10.1111/j.1365-246X.1995.tb03540.x

Kikuchi, M., & Kanamori, H. (1991). Inversion of complex body waves-III. *Bulletin of the Seismological Society of America*, *81*(6), 2335–2350. https://doi.org/10.1785/BSSA0810062335

Laske, G., Masters, T. G., Ma, Z., & Pasyanos, M. (2013). Update on CRUST1.0 - A 1-degree global model of Earth's crust. *Geophysical Research Abstracts*, *15*. Abstr. EGU2013-2658, 15, Abstract EGU2013–2658 https://igppweb.ucsd.edu/~gabi/crust1.html

Lay, T., Duputel, Z., Ye, L., & Kanamori, H. (2013). The December 7, 2012 Japan Trench intraplate doublet (*M*w 7.2, 7.1) and interactions between near-trench intraplate thrust and normal faulting. *Physics of the Earth and Planetary Interiors*, *220*, 73–78. https://doi.org/10.1016/j.pepi.2013.04.009

Lay, T., & Kanamori, H. (1980). Earthquake doublets in the Solomon Islands. *Physics of the Earth and Planetary Interiors*, *21*(4), 283–304. https://doi.org/10.1016/0031-9201(80)90134-X

Lomax, A. (2023). Precise, NLL-SSST-coherence hypocenter catalog for the 2023 *M*w 7.8 and *M*w 7.6 SE Turkey earthquake sequence. *Zenodo*. https://doi.org/10.5281/zenodo.7727678

Mai, P. M., Aspiotis, T., Aquib, T. A., Cano, E. V., Castro-Cruz, D., Espindola-Carmona, A., et al. (2023). The destructive earthquake doublet of 6 February 2023 in South-Central Türkiye and Northwestern Syria: Initial observations and analyses. *The Seismic Record*, *3*(2), 105–115. https://doi.org/10.1785/0320230007

McKenzie, D. (1972). Active tectonics of the Mediterranean region. *Geophysical Journal International*, *30*(2), 109–185. https://doi.org/10.1111/j.1365-246X.1972.tb02351.x

Melgar, D., Ganas, A., Taymaz, T., Valkaniotis, S., Crowell, B. W., Kapetanidis, V., et al. (2020). Rupture kinematics of 2020 January 24 *M*w 6.7 DoÄŸanyol-Sivrice, Turkey earthquake on the East Anatolian Fault Zone imaged by space geodesy. *Geophysical Journal International*, *223*(2), 862–874. https://doi.org/10.1093/gji/ggaa345

Melgar, D., Taymaz, T., Ganas, A., Crowell, B., Öcalan, T., Kahraman, M., et al. (2023). Sub- and super-shear ruptures during the 2023 *M*w 7.8 and *M*w 7.6 earthquake doublet in SE Türkiye. *Seismica*, *2*(3), 1–14. https://doi.org/10.26443/seismica.v2i3.387

Meng, L., Allen, R. M., & Ampuero, J.-P. (2014). Application of seismic array processing to earthquake early warning. *Bulletin of the Seismological Society of America*, *104*(5), 2553–2561. https://doi.org/10.1785/0120130277

Meng, L., Ampuero, J. P., Stock, J., Duputel, Z., Luo, Y., & Tsai, V. C. (2012). Earthquake in a maze: Compressional rupture branching during the 2012 *M*w 8.6 Sumatra earthquake. *Science*, *337*(6095), 724–726. https://doi.org/10.1126/science.1224030

Met Office. (2015). Cartopy: A cartographic python library with a Matplotlib interface. https://doi.org/10.5281/zenodo.1182735

Nissen, E., Elliott, J. R., Sloan, R. A., Craig, T. J., Funning, G. J., Hutko, A., et al. (2016). Limitations of rupture forecasting exposed by instantaneously triggered earthquake doublet. *Nature Geoscience*, *9*(4), 330–336. https://doi.org/10.1038/ngeo2653

Okubo, K., Rougier, E., Lei, Z., & Bhat, H. S. (2020). Modeling earthquakes with off-fault damage using the combined finite-discrete element method. *Computational Particle Mechanics*, *7*(5), 1057–1072. https://doi.org/10.1007/s40571-020-00335-4

Okuwaki, R., & Fan, W. (2022). Oblique convergence causes both thrust and strike-slip ruptures during the 2021 *M* 7.2 Haiti earthquake. *Geophysical Research Letters*, *49*(2), 1–12. https://doi.org/10.1029/2021GL096373

Okuwaki, R., Hicks, S. P., Craig, T. J., Fan, W., Goes, S., Wright, T. J., & Yagi, Y. (2021). Illuminating a contorted slab with a complex intraslab rupture evolution during the 2021 *M*w 7.3 East Cape, New Zealand earthquake. *Geophysical Research Letters*, *48*(24), 1–13. https://doi.org/10.1029/2021GL095117

Okuwaki, R., Hirano, S., Yagi, Y., & Shimizu, K. (2020). Inchworm-like source evolution through a geometrically complex fault fueled persistent supershear rupture during the 2018 Palu Indonesia earthquake. *Earth and Planetary Science Letters*, *547*, 116449. https://doi.org/10.1016/j.epsl.2020.116449

Okuwaki, R., Yagi, Y., Aránguiz, R., González, J., & González, G. (2016). Rupture process during the 2015 Illapel, Chile earthquake: Zigzag-along-dip rupture episodes. *Pure and Applied Geophysics*, *173*(4), 1011–1020. https://doi.org/10.1007/s00024-016-1271-6

Olson, A. H., & Apsel, R. J. (1982). Finite faults and inverse theory with applications to the 1979 Imperial Valley earthquake. *Bulletin of the Seismological Society of America*, *72*(6A), 1969–2001. https://doi.org/10.1785/BSSA07206A1969

Otsuki, K., & Dilov, T. (2005). Evolution of hierarchical self-similar geometry of experimental fault zones: Implications for seismic nucleation and earthquake size. *Journal of Geophysical Research*, *110*(3), 1–9. https://doi.org/10.1029/2004JB003359

Perinçek, D., & Çemen, I. (1990). The structural relationship between the East Anatolian and Dead Sea fault zones in southeastern Turkey. *Tectonophysics*, *172*(3–4), 331–340. https://doi.org/10.1016/0040-1951(90)90039-B

Pousse-Beltran, L., Nissen, E., Bergman, E. A., Cambaz, M. D., Gaudreau, É., Karasözen, E., & Tan, F. (2020). The 2020 *M*w 6.8 Elazığ (Turkey) earthquake reveals rupture behavior of the East Anatolian Fault. *Geophysical Research Letters*, *47*(13), 1–14. https://doi.org/10.1029/2020GL088136

Ragon, T., Simons, M., Bletery, Q., Cavalié, O., & Fielding, E. (2021). A stochastic view of the 2020 Elazığ *M*w 6.8 earthquake (Turkey). *Geophysical Research Letters*, *48*(3), 1–13. https://doi.org/10.1029/2020GL090704

Reitman, N. G., Briggs, R. W., Barnhart, W. D., Thompson Jobe, J. A., DuRoss, C. B., Hatem, A. E., et al. (2023). Preliminary fault rupture mapping of the 2023 *M* 7.8 and *M* 7.5 Türkiye Earthquakes. https://doi.org/10.5066/P985I7U2

Rosakis, A. J., Abdelmeguid, M., & Elbanna, A. (2023). Evidence of early supershear transition in the 6 February 2023 *M*w 7.8 Kahramanmaraş Turkey earthquake from near-field records. *EarthArXiv*. https://doi.org/10.31223/X5W95G

Ross, Z. E., Idini, B., Jia, Z., Stephenson, O. L., Zhong, M., Wang, X., et al. (2019). Hierarchical interlocked orthogonal faulting in the 2019 Ridgecrest earthquake sequence. *Science*, *366*(6463), 346–351. https://doi.org/10.1126/science.aaz0109

Ruppert, N. A., Rollins, C., Zhang, A., Meng, L., Holtkamp, S. G., West, M. E., & Freymueller, J. T. (2018). Complex faulting and triggered rupture during the 2018 *M*w 7.9 offshore Kodiak, Alaska, Earthquake. *Geophysical Research Letters*, *45*(15), 7533–7541. https://doi.org/10.1029/2018GL078931

Sato, D., Fukahata, Y., & Nozue, Y. (2022). Appropriate reduction of the posterior distribution in fully Bayesian inversions. *Geophysical Journal International*, *231*(2), 950–981. https://doi.org/10.1093/gji/ggac231

Satriano, C., Kiraly, E., Bernard, P., & Vilotte, J.-P. (2012). The 2012 *M*w 8.6 Sumatra earthquake: Evidence of westward sequential seismic ruptures associated to the reactivation of a N-S ocean fabric. *Geophysical Research Letters*, *39*(15), L15302. https://doi.org/10.1029/2012GL052387

Scholz, C. H., Ando, R., & Shaw, B. E. (2010). The mechanics of first order splay faulting: The strike-slip case. *Journal of Structural Geology*, *32*(1), 118–126. https://doi.org/10.1016/j.jsg.2009.10.007

Shimizu, K., Yagi, Y., Okuwaki, R., & Fukahata, Y. (2020). Development of an inversion method to extract information on fault geometry from teleseismic data. *Geophysical Journal International*, *220*(2), 1055–1065. https://doi.org/10.1093/gji/ggz496

Socquet, A., Hollingsworth, J., Pathier, E., & Bouchon, M. (2019). Evidence of supershear during the 2018 magnitude 7.5 Palu earthquake from space geodesy. *Nature Geoscience*, *12*(3), 192–199. https://doi.org/10.1038/s41561-018-0296-0

Tadapansawut, T., Okuwaki, R., Yagi, Y., & Yamashita, S. (2021). Rupture process of the 2020 Caribbean earthquake along the oriente transform fault, involving supershear rupture and geometric complexity of fault. *Geophysical Research Letters*, *48*(1), 1–9. https://doi.org/10.1029/2020GL090899

Taymaz, T., Eyidogan, H., & Jackson, J. (1991). Source parameters of large earthquakes in the East Anatolian Fault Zone (Turkey). *Geophysical Journal International*, *106*(3), 537–550. https://doi.org/10.1111/j.1365-246X.1991.tb06328.x

Taymaz, T., Ganas, A., Yolsal-Çevikbilen, S., Vera, F., Eken, T., Erman, C., et al. (2021). Source mechanism and rupture process of the 24 January 2020 *M*w 6.7 DoÄŸanyol-Sivrice earthquake obtained from seismological waveform analysis and space geodetic observations on the east Anatolian fault zone (Turkey). *Tectonophysics*, *804*, 228745. https://doi.org/10.1016/j.tecto.2021.228745

Taymaz, T., Jackson, J., & McKenzie, D. (1991). Active tectonics of the north and central Aegean Sea. *Geophysical Journal International*, *106*(2), 433–490. https://doi.org/10.1111/j.1365-246X.1991.tb03906.x

Taymaz, T., Westaway, R., & Reilinger, R. (2004). Active faulting and crustal deformation in the Eastern Mediterranean region. *Tectonophysics*, *391*(1–4), 1–9. https://doi.org/10.1016/j.tecto.2004.07.005

ten Brink, U., Wei, Y., Fan, W., Granja-Bruña, J.-L., & Miller, N. (2020). Mysterious tsunami in the Caribbean Sea following the 2010 Haiti earthquake possibly generated by dynamically triggered early aftershocks. *Earth and Planetary Science Letters*, *540*, 116269. https://doi.org/10.1016/j.epsl.2020.116269

Trugman, D. T., & Dunham, E. M. (2014). A 2D pseudodynamic rupture model generator for earthquakes on geometrically complex faults. *Bulletin of the Seismological Society of America*, *104*(1), 95–112. https://doi.org/10.1785/0120130138

Vallée, M., Xie, Y., Grandin, R., Villegas-Lanza, J. C., Nocquet, J. M., Vaca, S., et al. (2023). Self-reactivated rupture during the 2019 *M*w=8 northern Peru intraslab earthquake. *Earth and Planetary Science Letters*, *601*, 117886. https://doi.org/10.1016/j.epsl.2022.117886

Wei, S., Fielding, E., Leprince, S., Sladen, A., Avouac, J.-P., Helmberger, D., et al. (2011). Superficial simplicity of the 2010 El Mayor-Cucapah earthquake of Baja California in Mexico. *Nature Geoscience*, *4*(9), 615–618. https://doi.org/10.1038/ngeo1213

Weiss, J. R., Walters, R. J., Morishita, Y., Wright, T. J., Lazecky, M., Wang, H., et al. (2020). High-resolution surface velocities and strain for Anatolia from Sentinel-1 InSAR and GNSS data. *Geophysical Research Letters*, *47*(17), e2020GL087376. https://doi.org/10.1029/2020GL087376

Wessel, P., & Luis, J. F. (2017). The GMT/MATLAB toolbox. *Geochemistry, Geophysics, Geosystems*, *18*(2), 811–823. https://doi.org/10.1002/2016GC006723

Xu, S., Fukuyama, E., Ben-Zion, Y., & Ampuero, J.-P. (2015). Dynamic rupture activation of backthrust fault branching. *Tectonophysics*, *644–645*, 161–183. https://doi.org/10.1016/j.tecto.2015.01.011

Xu, Y., Koper, K. D., Sufri, O., Zhu, L., & Hutko, A. R. (2009). Rupture imaging of the *M*w 7.9 12 May 2008 Wenchuan earthquake from back projection of teleseismic P waves. *Geochemistry, Geophysics, Geosystems*, *10*(4), Q04006. https://doi.org/10.1029/2008GC002335

Yabuki, T., & Matsu'ura, M. (1992). Geodetic data inversion using a Bayesian information criterion for spatial distribution of fault slip. *Geophysical Journal International*, *109*(2), 363–375. https://doi.org/10.1111/j.1365-246X.1992.tb00102.x

Yagi, Y., & Fukahata, Y. (2011). Introduction of uncertainty of Green's function into waveform inversion for seismic source processes. *Geophysical Journal International*, *186*(2), 711–720. https://doi.org/10.1111/j.1365-246X.2011.05043.x

Yagi, Y., Okuwaki, R., Enescu, B., & Lu, J. (2023). Irregular rupture process of the 2022 Taitung, Taiwan, earthquake sequence. *Scientific Reports*, *13*(1), 1107. https://doi.org/10.1038/s41598-023-27384-y

Yamashita, S., Yagi, Y., & Okuwaki, R. (2022). Irregular rupture propagation and geometric fault complexities during the 2010 *M*w 7.2 El Mayor-Cucapah earthquake. *Scientific Reports*, *12*(1), 4575. https://doi.org/10.1038/s41598-022-08671-6

Yamashita, S., Yagi, Y., Okuwaki, R., Shimizu, K., Agata, R., & Fukahata, Y. (2022). Potency density tensor inversion of complex body waveforms with time-adaptive smoothing constraint. *Geophysical Journal International*, *231*(1), 91–107. https://doi.org/10.1093/gji/ggac181

Yao, H., Gerstoft, P., Shearer, P. M., & Mecklenbräuker, C. (2011). Compressive sensing of the Tohoku-Oki *M*w 9.0 earthquake: Frequency-dependent rupture modes. *Geophysical Research Letters*, *38*(20), L20310. https://doi.org/10.1029/2011GL049223

Yıkılmaz, M. B., Turcotte, D. L., Heien, E. M., Kellogg, L. H., & Rundle, J. B. (2015). Critical jump distance for propagating earthquake ruptures across step-overs. *Pure and Applied Geophysics*, *172*(8), 2195–2201. https://doi.org/10.1007/s00024-014-0786-y

Zahradník, J., Turhan, F., Sokos, E., & Gallovič, F. (2023). Asperity–like (segmented) structure of the 6 February 2023 Turkish earthquakes. *EarthArXiv*, 1–20. https://doi.org/10.31223/X5T666

References From the Supporting Information

King, G. C., Stein, R. S., & Lin, J. (1994). Static stress changes and the triggering of earthquakes. *Bulletin of the Seismological Society of America*, *84*(3), 935–953. https://doi.org/10.1785/BSSA0840030935

Lin, J., & Stein, R. S. (2004). Stress triggering in thrust and subduction earthquakes and stress interaction between the southern San Andreas and nearby thrust and strike-slip faults. *Journal of Geophysical Research*, *109*(B2), 1–19. https://doi.org/10.1029/2003jb002607

Toda, S., Stein, R. S., Richards-Dinger, K., & Bozkurt, S. B. (2005). Forecasting the evolution of seismicity in southern California: Animations built on earthquake stress transfer. *Journal of Geophysical Research*, *110*(5), 1–17. https://doi.org/10.1029/2004JB003415

Wang, J., Xu, C., Freymueller, J. T., Wen, Y., & Xiao, Z. (2021). AutoCoulomb: An automated configurable program to calculate Coulomb stress changes on receiver faults with any orientation and its application to the 2020 *M*w 7.8 Simeonof Island, Alaska, Earthquake. *Seismological Research Letters*, *92*(4), 2591–2609. https://doi.org/10.1785/0220200283